3D PRINTING TECHNOLOGY AS THE MANUFACTURING METHOD OF COMPLEX EXOSKELETON ELEMENTS CARRYING HEAVY LOADS

Dawid CEKUS*, Tomasz DOMAŃSKI*, Marcin SKOTNICZNY*, Paweł KWIATOŃ*, Jolanta POZORSKA**

*Faculty of Mechanical Engineering, Czestochowa University of Technology,
al. Armii Krajowej 21, 42-201 Częstochowa, Poland
**Faculty of Control, Robotics and Electrical Engineering, Institute of Mathematics,
Poznan University of Technology, Piotrowo 3a, 61-138 Poznań, Poland

dawid.cekus@pcz.pl, tomasz.domanski@pcz.pl, marcin.skotniczny@pcz.pl, pawel.kwiaton@pcz.pl, jolanta.pozorska@put.poznan.pl

received 13 July 2026, revised 16 July 2026, accepted 20 July 2026

Abstract: This article describes one of the challenges encountered when designing high-load components manufactured using 3D printing technology: material anisotropy. Using a lower-limb exoskeleton as a reference, the advantages and limitations of 3D printing were compared with those of conventional machining of metal components. The tensile strength was examined for PA6-CF specimens printed in the longitudinal and transverse directions, both before and after annealing. The experimentally determined orthotropic material properties were incorporated into finite element models of the exoskeleton joint to evaluate the influence of material anisotropy on structural safety under nominal and peak loading conditions. The simulations demonstrated that the printed components remain safe under the rated motor torque, whereas higher overloads primarily threaten the interlayer (Z-direction) strength and require design or control-system limitations. The results indicate that print orientation and annealing affect the load-bearing capacity of the printed components, while the Z direction remains the most critical due to interlayer bonding.

Key words: 3D printing, exoskeleton, heavy loads, static analysis

1. INTRODUCTION

When designing machines, robots, mechanisms, or mechatronic systems, designers strive to minimize construction costs without compromising fundamental design requirements, such as structural strength. Depending on the type of machine, additional requirements may include reducing the structure's weight and volume, adapting it to its surroundings, and accounting for dynamic loads.

For stationary industrial machines, designers are usually not significantly constrained by weight, dimensions, or additional loads acting on the system. In mobile robots, however, the mass of the mechanism must be supported by both the structure and the drive system, while dimensional limitations may also arise. Walking robots are additionally subjected to dynamic loads during motion, and increasing the structural mass leads to higher stresses. Humanoid walking robots face further dimensional constraints because the entire mechanism should remain within the humanoid outline [1].

One of the most demanding systems in this respect is the exoskeleton. Its dimensional requirements are even more stringent because the mechanism must also accommodate the user's body. Any increase in size may negatively affect user comfort. Furthermore, because the exoskeleton interacts directly with the user's body, high structural strength is required to minimize the risk of injury during operation [2–4].

Certain mechanisms require significant reductions in volume and weight while maintaining appropriate mechanical properties. Meeting these requirements often leads to components with complex geometries. Although such components may satisfy the requirements of numerical simulations, their manufacturing process may be multi-stage and costly. For complex geometries, production from semi-finished products, such as tubes or rods, may also be impossible. In such cases, machining from a solid metal block may be necessary, further increasing costs because of the long processing time and substantial material waste [5,6].

Currently, one of the methods for manufacturing components with advanced geometry is 3D printing, such as FFF (Fused Filament Fabrication). This technology enables the production of parts with minimal material waste while eliminating the need for molds, including injection molds. The cost of 3D printers is also significantly lower than the cost of machines used in traditional manufacturing processes, such as plastic injection molding. Therefore, it can be concluded that 3D printing enables significant cost reductions in single-unit or small-scale production, which favors its use in the design of personalized exoskeletons and lower-limb orthoses [6-8].

However, the FFF method also has certain limitations. One of the main limitations is the material's anisotropy. During static tensile testing, specimens with layers aligned in the direction of stretching typically exhibit better strength parameters. When the print layers are aligned perpendicular to the stretching direction, strength properties can decrease significantly [9-11].

Another issue is the use of carbon fiber-reinforced materials. Studies have shown that the mechanical properties of such composites depend, among other things, on the fiber mass fraction, their

DOI: 10.65731/ama/2026-0075

orientation, and the representation of material anisotropy in the computational model [10-13].

Although 3D printing has already been used in exoskeletons and orthoses, the verification of the strength of highly loaded exoskeleton joint components made of carbon fiber-reinforced polyamide, based on experimentally determined anisotropic material properties, is still insufficiently described. This study aims to assess the applicability of 3D printing technology for manufacturing geometrically complex lower-limb exoskeleton joint components capable of carrying high loads, taking into account the anisotropic properties of PA6-CF material and their influence on structural safety. Specifically, the objectives were to:

- determine the direction-dependent mechanical properties of PA6-CF specimens before and after annealing;
- define orthotropic material models based on the experimental results;
- assess the structural safety of selected exoskeleton joint components under rated and peak torque loads; and
- identify a torque range for which the experimentally determined tensile-strength limits are not exceeded.

2. MODEL DESCRIPTION

The analyzed model represents one of the assemblies of a lower-limb exoskeleton under construction (Fig. 1). The analysis focused on elements subjected to the highest loads: the connecting rectangular steel profiles that support the movement of the human femur and tibia (thus replacing the joint). The joint under consideration consists of two main sleeves that can rotate relative to each other. A motor is mounted inside the inner sleeve (Fig. 2a) to drive the exoskeleton. Torque is transmitted to the outer sleeve (Fig. 2b) through two components: the coupling sleeve (Fig. 2c) and the crosspiece (Fig. 2d).

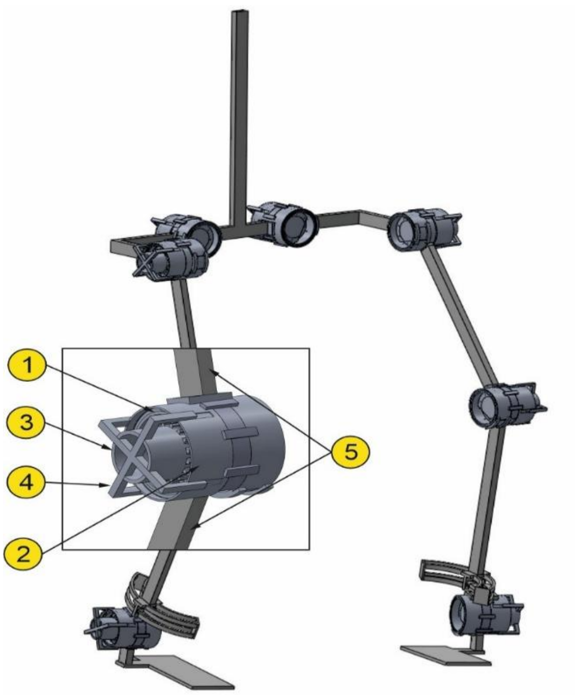

Fig. 1. Analyzed model: 1 – inner sleeve, 2 – outer sleeve, 3, 4 – elements transmitting motion from the inner sleeve to the outer sleeve, 5 – steel rectangular profiles

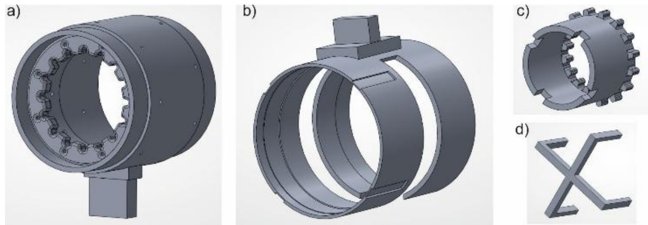

Fig. 2. Basic joint components: a) inner sleeve, b) outer sleeve, c) coupling sleeve, d) cross-shaped coupling element

The outer sleeve is exposed to significant loads resulting from the weight of the supported components and the torque generated by the motor shaft. Additionally, the proposed design includes a large cutout in the center, allowing limb rotation and mounting tabs. Manufacturing such a sleeve using conventional subtractive machining methods would require multiple technological steps and result in significant material waste, increasing production costs.

The coupling sleeve and the crosspiece are also subject to high loads and may be prone to damage. These components transmit the torque generated by the motor between the main joint sleeves, which results in significant stresses within them. The coupling sleeve, like the outer sleeve, should be manufactured using additive manufacturing due to its shape. In the case of the crosspiece, which has a simple geometry, conventional manufacturing methods can be used, for example, with steel as the material.

This approach requires the strength of the printed components to be verified numerically as the first step. To accurately reproduce the properties of the actual object in simulation tests, it was necessary to obtain characteristics of the material from which the sleeves would be printed. For this purpose, a static tensile test was conducted in accordance with ISO 527.

3. MATERIAL TEST

The components were printed on an Ultimaker S5 printer in a closed configuration with a material station using PolyMide PA6-CF filament, a carbon fiber-reinforced nylon filament. PolyDis-solve S1 filament was used as support material, and Magigoo PRO PA was used to ensure adhesion to the printer's glass substrate.

Static tensile test specimens were prepared for four test series. The test series differed in print orientation and heat-treatment condition. Series 1 included unannealed specimens printed in the longitudinal direction, Series 2 included unannealed specimens printed in the transverse direction, Series 3 included annealed specimens printed in the longitudinal direction, and Series 4 included annealed specimens printed in the transverse direction. Three specimens were tested in each series. The specimens were printed in two directions to determine tensile strength in the longitudinal (at a 45° angle) and transverse directions relative to the direction of subsequent 3D print layers, as well as before and after oven heating. These specimens are shown in Fig. 3-6.

An FCF 2.5SM muffle furnace with an MRT-7B temperature controller was used to heat the specimens. The printing and heat-treatment parameters were adopted from the filament technical data sheet [14] and presented in Table 1.

Tab. 1. Printing and heating parameters

Nozzle diameter	0.4 mm
Printing temperature	280°C
Printing speed	45 mm/s
Layer thickness	0.2 mm
Infill density	100%
Infill pattern	Linear, 45°
Annealing temperature	100°C
Annealing time	7 h

During tensile testing of the printed specimens, repeated fractures occurred outside the gauge length. These results were included for comparative purposes, while specimens that fractured correctly were analyzed separately. Only specimens that fractured within the gauge length were included in the calculation of mean values. In Tables 2–5, bold values indicate specimens that fractured within the gauge length and were included in the calculation of the mean values. Due to the limited number of valid specimens in some series, the results should be treated as preliminary. In the first stage, a static tensile test was performed on as-printed specimens, with the layer deposition path parallel to the tensile force vector (Fig. 3, Table 2).

Fig. 3. Fracture location for unannealed specimens (longitudinal direction)

Tab. 2. Strength parameters for unannealed specimens (longitudinal direction)

No specimen	E (GPa)	$R_{0,2}$ (MPa)	R_m (MPa)	Elonga-tion (mm)	Necking (mm)
No. 1	**3.92**	**73.1**	**88.0**	**2.3**	**0.262**
No. 2	**3.66**	**71.4**	**85.6**	**2.0**	**0.215**
No. 3	3.74	71.1	77.4	1.1	0.222
Average	3.79	72.21	86.81	2.14	0.239

Analysis of the test results shows significant dispersion in Young's modulus values among individual test specimens. These discrepancies may result directly from the geometric repeatability and structural quality of the 3D prints, as well as from local variations in the packing of the carbon fibers reinforcing the filament matrix. The manufacturer's technical data sheet also indicates that this material may be sensitive to variations in this parameter [14].

In the next stage, reference specimens (without annealing) were analyzed, with subsequent layers applied parallel to the tensile force vector (Fig. 4, Table 3).

Fig. 4. Fracture location for unannealed specimens (transverse direction)

Tab. 3. Strength parameters for unannealed specimens (transverse direction)

No specimen	E (GPa)	$R_{0,2}$ (MPa)	R_m (MPa)	Elonga-tion (mm)	Necking (mm)
No. 4	2.99	31.6	33.1	0.7	0.09
No. 5	**2.65**	**29.1**	**32.8**	**0.7**	**0.07**
No. 6	2.77	31.0	31.0	0.7	0.092
Average	**2.8**	**29.1**	**32.8**	**0.7**	**0.07**

In the second tensile-test series, only specimen no. 5 fractured within the gauge length. As in the previous case, this specimen also showed the highest Young's modulus.

The next tensile-test series was performed on annealed specimens in which the layer-deposition direction was aligned with the tensile-loading direction (Fig. 5, Table 4).

Fig. 5. Fracture location for annealed specimens (longitudinal direction)

Tab. 4. Strength parameters for annealed specimens (longitudinal direction)

No specimen	E (GPa)	$R_{0,2}$ (MPa)	R_m (MPa)	Elongation (mm)	Necking (mm)
No. 7	**4.47**	**77.9**	**95.1**	**1.8**	**0.455**
No. 8	**4.71**	75.1	77.2	0.9	0.387
No. 9	4.38	75.5	80.3	1.0	0.418
Average	4.52	**77.9**	**95.1**	**1.8**	**0.455**

In the analyzed series, specimen no. 7 failed directly adjacent to the boundary of the gauge length, while the remaining specimens fractured completely outside the gauge length. Consistent with previous observations, the specimen fractured within the gauge length and exhibited the highest Young's modulus, tensile strength (Rm), and relative elongation at break.

The final test series involved annealed specimens with the layer direction oriented perpendicular to the tensile loading direction (Fig. 6, Table 5).

Fig. 6. Fracture location for annealed specimens (transverse direction)

Tab. 5. Strength parameters for annealed specimens (transverse direction)

No specimen	E (GPa)	$R_{0,2}$ (MPa)	R_m (MPa)	Elongation (mm)	Necking (mm)
No. 10	**2.84**	**29.94**	**33.8**	**0.6**	**0.098**
No. 11	2.82	27.98	31.8	0.6	0.156
No. 12	**2.69**	**28.93**	**32.0**	**0.6**	**0.11**
Average	2.78	28.93	32.85	0.6	0.104

In the final series, specimen no. 11 cracked outside the gauge length. The remaining specimens were used to determine the mean values of the strength parameters.

Table 6 presents the mean values for each test series (specimens broken outside the gauge length are not averaged), while Fig. 7 shows the course of the static tensile test.

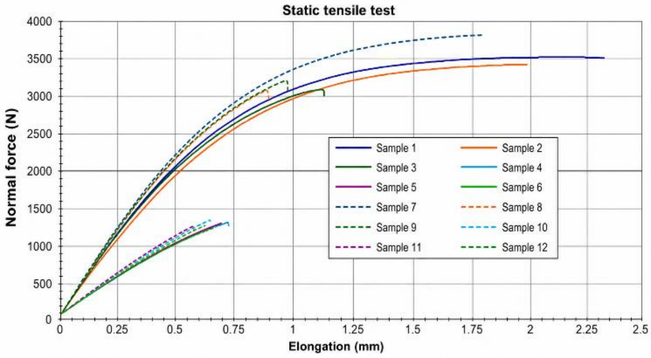

Fig. 7. Normal Force – Elongation graph for static tensile test

Tab. 6. Comparison of strength parameters for all test series

No series	E (GPa)	$R_{0,2}$ (MPa)	R_m (MPa)	Elongation (mm)	Necking (mm)
Series 1	3.79	72.21	86.81	2.14	0.239
Series 2	2.80	29.1	32.8	0.7	0.07
Series 3	4.52	77.9	95.1	1.8	0.455
Series 4	2.78	28.93	32.85	0.6	0.104

Analysis of the presented results indicates significant scatter in the measured values obtained for the tested material. This observation is fully consistent with expectations, as the filament manufacturer's technical specifications define acceptable tolerance ranges for individual mechanical properties. Despite the observed scatter, the experimental results allow clear structural conclusions to be formulated.

First, it is important to note the distinct anisotropies in mechanical properties with respect to the orientation of the print paths. Specimens with layers oriented parallel to the loading axis exhibited a higher Young's modulus, yield strength ($R_{0.2}$), and higher tensile strength (R_m) compared to specimens with a transverse layer orientation.

Another regularity is the significant increase in Young's modulus observed for heat-treated (annealed) specimens with a longitudinal orientation, compared to reference (unannealed) specimens with the same structural configuration. The results also indicate a trend toward increased tensile strength with annealing, but verification of this hypothesis requires testing more specimens. The conclusion concerns the marginal effect of heat treatment on the strength properties of specimens in which the layers were oriented perpendicular to the tensile force vector.

Tab. 7. Comparison of strength parameters between tests and technical data sheet

	E (GPa)		R_m (MPa)	
	Measurement	Catalog	Measurement	Catalog
Series 1	3.79	5.66±0.47	86.81	81.7±6
Series 2	2.8	4.71±0.28	32.8	64.4±5.6
Series 3	4.52	7.45±0.66	95.1	105±5
Series 4	2.78	4.35±0.2	32.85	67.7±4.7

To precisely determine the Poisson's ratio, a static tensile test was also performed for the four series described in the previous section. A resistance strain gauge type TF-5-2x/120 with a resistance of 120 ± 0.2 Ω was attached to the printed specimens (Fig. 8). The values obtained from the tests are presented in Table 8.

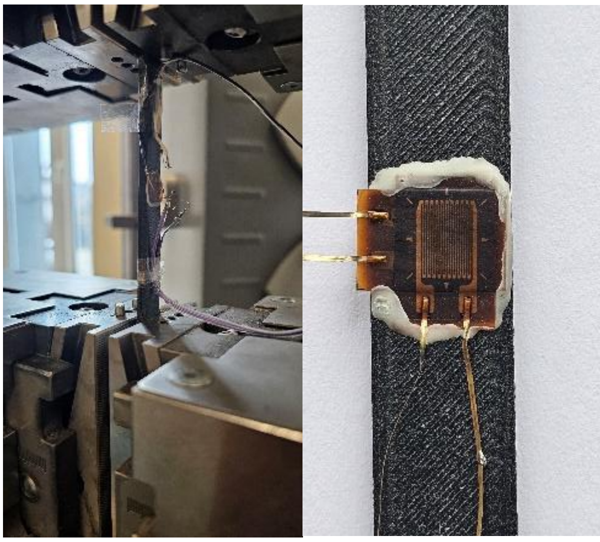

Fig. 8. Tensile test with a resistance strain gauge

Tab. 8. Experimental values of Poisson's ratio

No series	Poisson's ratio
Series 1	0.5
Series 2	0.26
Series 3	0.47
Series 4	0.23

Analysis of the above table indicates that the obtained strength parameters differ significantly from the values provided in the technical data sheet. The Young's modulus determined by the manufacturer is higher than the experimental value. For specimens printed parallel to the loading direction, the differences in tensile strength relative to the catalog data are small. In contrast, for specimens oriented perpendicular to the loading direction, they are significant. This may indicate the possibility of improving the printing process to increase the strength of printed elements in the interlayer direction.

The observed differences may be due to printer and printing process parameters, such as nozzle diameter, layer thickness, nozzle and print bed temperature, printing speed, cooling settings, and fill pattern. This means that a more comprehensive assessment of 3D printing technology's capabilities requires further research to determine how these parameters affect print durability.

4. NUMERICAL TESTS

Numerical strength tests were conducted in SolidWorks. The FEM computational model was prepared to accurately represent the operating conditions of the analyzed system while enabling efficient numerical calculations. Therefore, only three elements were included in the analysis (Fig. 9): the coupling sleeve (a), the cross-piece (b), and the outer sleeve (c). The numerical model assumptions were defined to reproduce the operating conditions of the analyzed joint while limiting the computational cost. The adopted boundary conditions, loading conditions, contact definition, and material assignments are described below.

Other elements of the exoskeleton joint, such as the motor, bearings, the inner sleeve, and standardized elements, were omitted. This was due to their geometry, material, and position in the system, which indicated that they should not fail before the elements included in the analysis.

The interacting elements in the computational model were connected using a global surface-to-surface contact set. This contact prevents interpenetration of the elements, regardless of their initial contact state, while allowing gaps to form between them. In this case, it was not necessary to define additional local contacts.

The following boundary conditions (Fig. 9) were introduced in the calculation model:

- roller/sliding restraint was applied to the upper surface of the coupling element (1) and to the four planes of the outer sleeve (6). In the case of the cross, this condition prevents displacement in a direction perpendicular to the specified plane, while in the case of the outer sleeve, this constraint reflects the action of the element that prevents the sleeve from spreading in a real system; the roller/sliding restraint condition simultaneously allows the specified surface to contract or expand under load;
- the two inner cylindrical surfaces of the outer sleeve were prevented from moving in the radial and axial directions (2), corresponding to the bearings being mounted in these locations; a similar constraint was applied to one outer cylindrical surface of the sleeve transmitting torque from the motor (4), representing the presence of the bearing and other components not included in the calculation model;
- a remote mass (3) was used, which represents the load on the joint caused by the displaced limb, i.e., the calf; the mass point was assumed to be located at the center of mass of the analyzed limb fragment, according to the local coordinate system: x = −22 mm, y = −220 mm, z = −12 mm; the mass value was assumed to be 20 kg;
- a torque (5), generated by the motor, was applied to the inner cylindrical surface;
- the effect of gravity (7) was also included in the model.

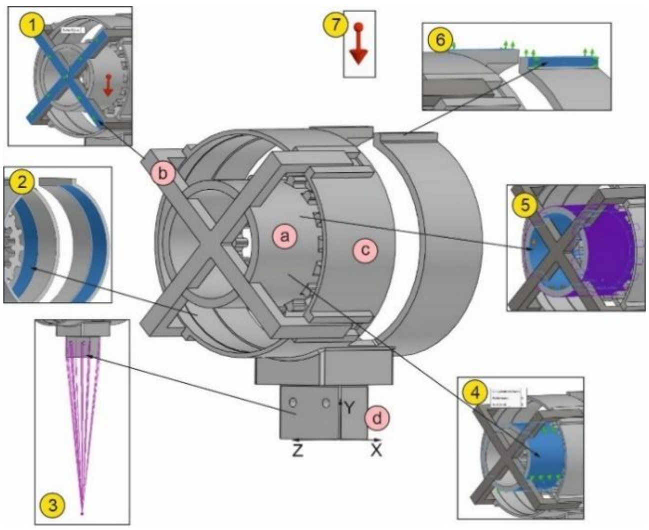

Fig. 9. Geometric model and adopted boundary conditions

 DOI: 10.65731/ama/2026-0075

The material test results presented in the previous chapter were used to define two new orthotropic materials with a linear-elastic behavior model. These materials were assigned to the outer sleeve (Fig. 9c) and the coupling sleeve (Fig. 9a) according to the adopted coordinate system (Fig. 9d), which corresponds to the 3D printing method used for the individual elements.

For the crosspiece (Fig. 9b), the element was assumed to be made of AISI 304 steel. When defining the material data, the Max von Mises Stress criterion was selected as the default failure criterion. Among the criteria available in SolidWorks for solid bodies, this was the most appropriate for the case analyzed. Due to its shape and size, the model could not be defined as a multilayer composite shell containing 2 to 50 layers.

The adopted material parameters are summarized in Table 9. Column I presents the values obtained for the specimens without annealing, while column II presents the values determined after annealing. Columns III and IV present the catalog values for the material without annealing and after annealing, respectively.

Tab. 9. Comparison of strength parameters between tests and technical data sheet [14]

Properties	I	II	III	IV
Elastic Modulus in X (MPa)	3790	2800	5660	7450
Elastic Modulus in Y (MPa)	3790	2800	5660	7450
Elastic Modulus in Z (MPa)	4520	2780	4710	4350
Poisson's Ratio in XY	0.5	0.47	0.30	0.37
Poisson's Ratio in YZ	0.26	0.23	0.33	0.40
Poisson's Ratio in XZ	0.26	0.23	0.28	0.35
Mass Density (kg/m3)	1020	1020	1170	1170
Tensile Strength in X (MPa)	86.61	95.1	81.7	105
Tensile Strength in Y (MPa)	86.61	95.1	81.7	105
Tensile Strength in Z (MPa)	32.8	32.85	64.4	67.7
Yield Strength	29.1	28.95	45	65

As noted in the previous chapter, experimentally obtained material data in most cases significantly differ from the manufacturer's catalog data. It is also important to note that the experimentally determined strength parameters are usually lower than the catalog values. This means that uncritically adopting the manufacturer's data can lead to an overestimation of the load-bearing capacity of the printed components and, consequently, to their failure earlier than would be expected from an analysis based on catalog data.

For this reason, simulation studies of the designed structure were conducted exclusively using experimental data. The computational model in all analyzed cases consisted of 824,049 nodes, 533,619 elements, and 2,499,501 degrees of freedom. A mesh-convergence study was performed by gradually refining the finite element mesh and comparing the maximum stress values in the critical regions. Further mesh refinement resulted in only minor changes in the calculated stress values, confirming that the adopted mesh provided a satisfactory compromise between numerical accuracy and computational cost. The computational time for each case was approximately 17 minutes on a computer equipped with an AMD Ryzen AI 9 HX processor, 32 GB of RAM, and an NVIDIA GeForce RTX graphics card with 8 GB of VRAM.

Figures 10, 11, 14, and 16 show the distribution of reduced stresses according to the von Mises hypothesis. In contrast, Figures 12, 13, 15, and 17 show the distribution of normal stresses in the X, Y, and Z directions, as defined by the adopted local coordinate system (Fig. 9d).

The analyses were conducted for two torque values generated by the motor: a rated torque of 48 Nm and a maximum torque of 120 Nm. The results for the rated torque are presented in Figures 10–13, and the results for the maximum torque are presented in Figures 14–17.

Figures 10, 12, 14, and 15 refer to the model in which the sleeves were assigned the properties of the unannealed material. Figures 11, 13, 16, and 17 present the results for sleeves made from the annealed material.

The highest values of reduced stresses occurred in the steel crosspiece. However, in none of the analyzed cases did they exceed the permissible values for this material. Therefore, the crosspiece and the finite element mesh were omitted from the figures showing the normal stress distributions to improve the readability of the results for the sleeves. The isochromatic ranges were selected according to the material properties assigned to the sleeves.

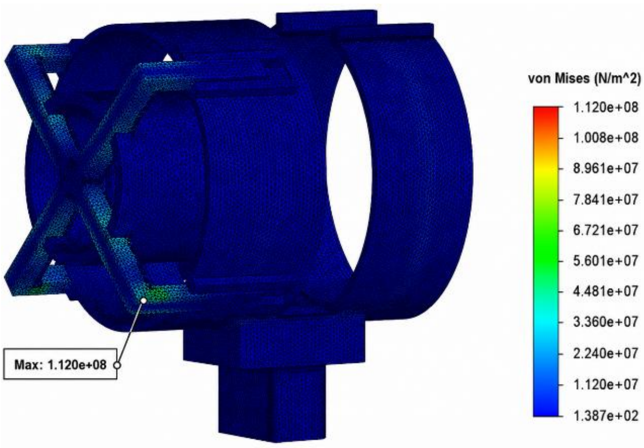

Fig. 10. Distribution of von Mises stress in the system subjected to a rated torque of 48 Nm – sleeves made of unannealed material

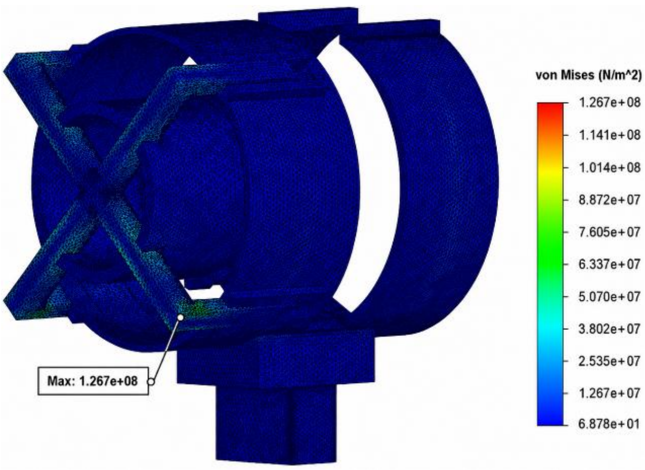

Fig. 11. Distribution of von Mises stress in the system subjected to a rated torque of 48 Nm – sleeves made of annealed material

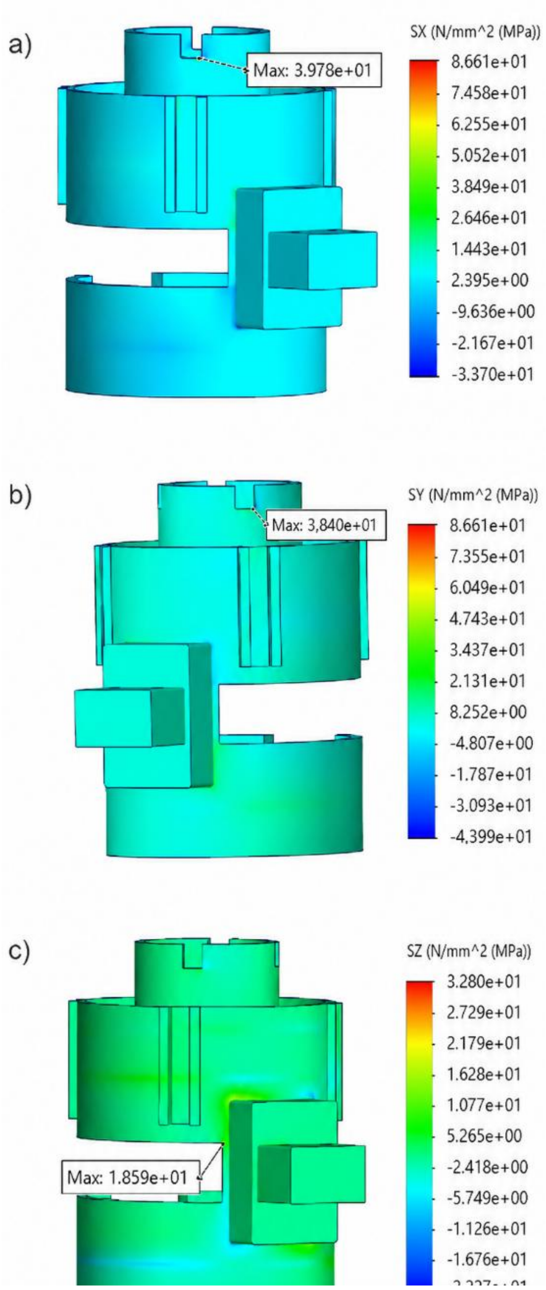

Fig. 12. Normal stress in the X (a), Y (b), and Z (c) directions in the system loaded with a rated torque of 48 Nm – sleeves made of unannealed materia

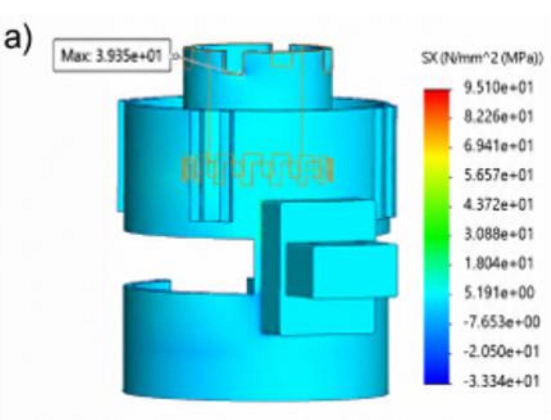

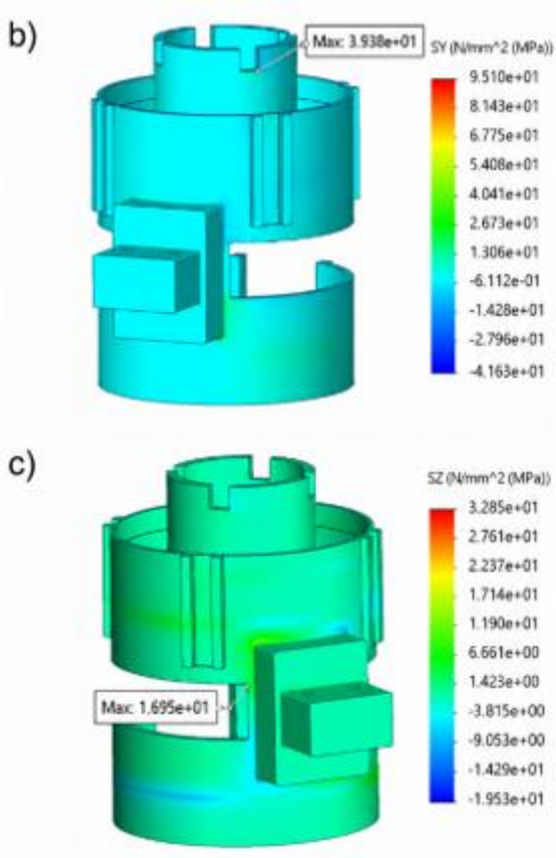

Fig. 13. Normal stress distribution in the X (a), Y (b), and Z (c) directions in the system subjected to a rated torque of 48 Nm – sleeves made of annealed material

When subjected to a torque of 48 Nm, the results indicate that the printed components should not be damaged, whether annealed or analyzed in their unannealed state. Normal stresses in the X, Y, and Z directions do not exceed the tensile strength values determined for these directions. Higher maximum reduced stresses in the crosspiece occur in the annealed configuration. However, for printed components, higher stress values are observed in the unannealed configuration. The locations of the maximum stress areas are similar in both material variants. For normal stresses in the X and Y directions, the highest values occur in the coupling sleeve at the contact zone with the crosspiece, whereas in the Z direction, the highest values occur in the outer sleeve.

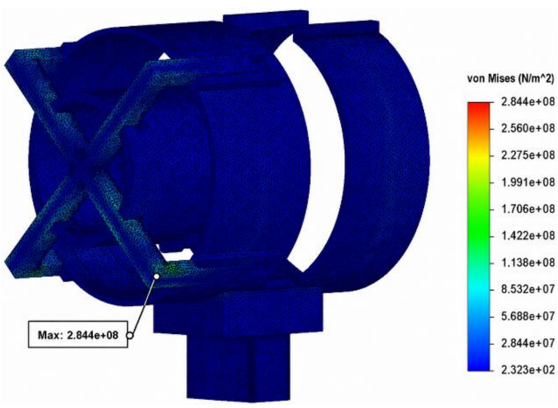

Fig. 14. Distribution of von Mises stress in the system subjected to a peak torque of 120 Nm – sleeves made of unannealed material

DOI: 10.65731/ama/2026-0075

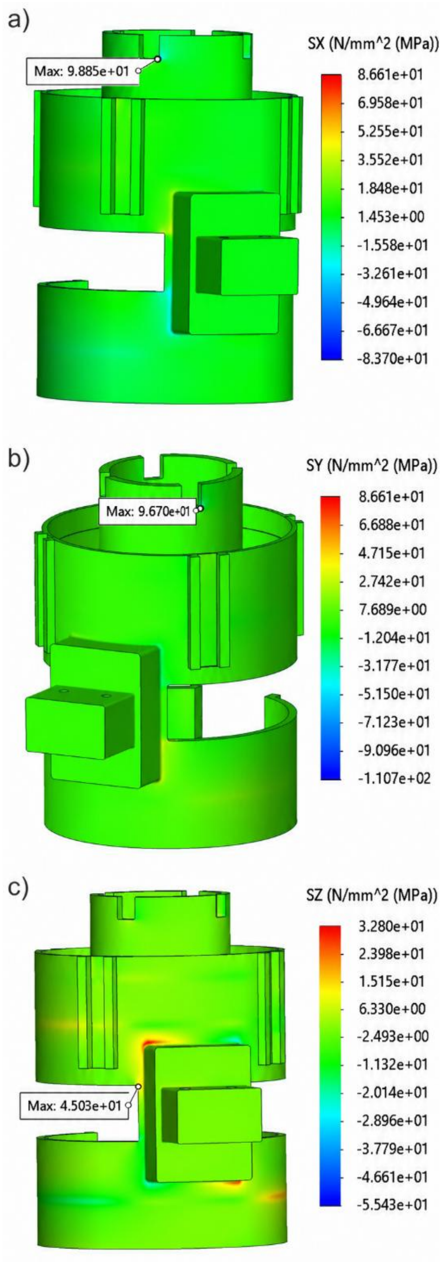

Fig. 15. Distribution of normal stress in the X (a), Y (b), and Z (c) directions in the system subjected to a peak torque of 120 Nm – sleeves made of unannealed material

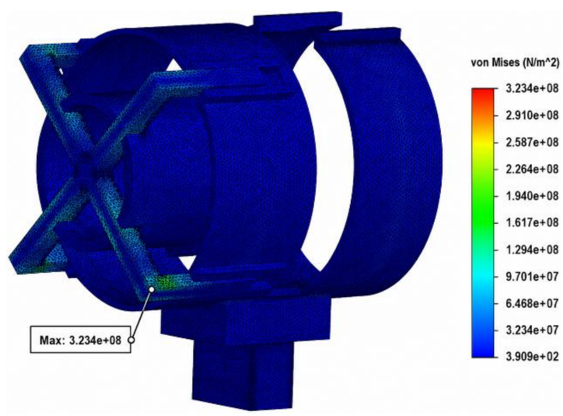

Fig. 16. Distribution of von Mises stress in the system subjected to a peak torque of 120 Nm – sleeves made of annealed material

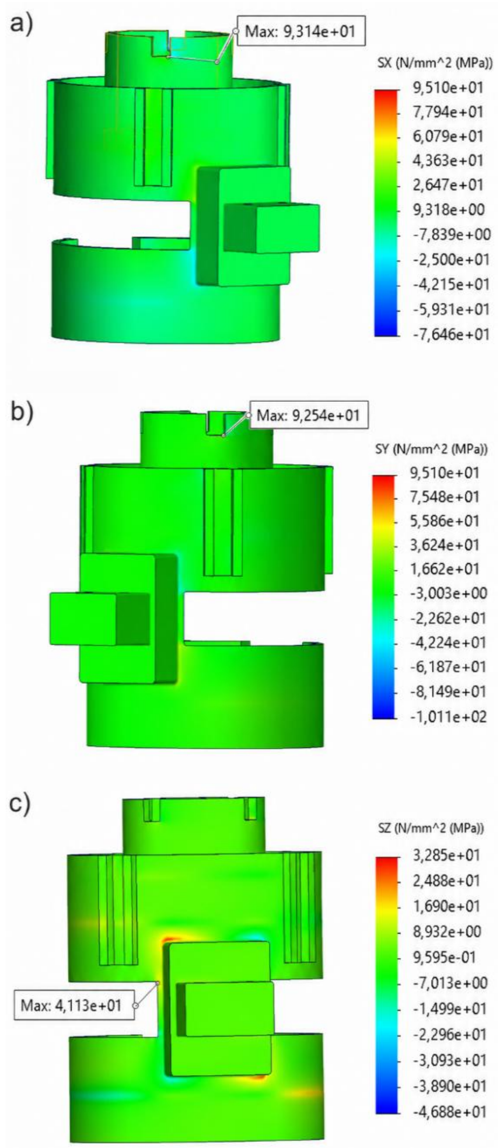

Fig. 17. Distribution of normal stress in the X (a), Y (b), and Z (c) directions in the system subjected to a peak torque of 120 Nm – sleeves made of annealed material

For a torque load of 120 Nm, which occurs only momentarily in the system during peak overload conditions, the locations of maximum stress values are the same for the annealed and unannealed material. These areas also coincide with the stress concentrations observed for the 48 Nm torque load. However, in this case, the printed components may be damaged because the tensile strength limits are exceeded. For the unannealed components, the limits are exceeded in the X and Y directions, while in the Z direction, they are exceeded for both the unannealed and annealed materials. To determine the torque value at which the tensile strength limits are exceeded, an additional design analysis was performed. The system load was varied from 58 Nm to 108 Nm in 10 Nm increments. The results are summarized in Table 10.

The results indicate that, for both material variants (unannealed and annealed), a safe system load is a motor torque of 88 Nm. At this value, the tensile strength limits are not exceeded. For higher torque values, it is advisable to use annealed components and carefully monitor the system's response in the Z-axis direction, where the risk of exceeding the limits is greatest. An alternative solution may be to properly configure the control system to limit the motor's maximum torque to levels safe for the printed components.

Tab. 10. Maximum normal stresses in the X, Y, and Z directions under different torque values

Moment (Nm)	Unannealed material			Annealed material		
	Max normal stress (MPa) in direction					
	X	Y	Z	X	Y	Z
58	50.18	49.93	20.68	45.25	44.50	19.92
68	58.77	58.68	24.07	52.99	52.26	23.19
78	67.30	67.31	27.46	60.70	60.01	26.47
88	75.86	76.00	30.84	68.40	67.72	29.74
98	84.47	84.78	34.23	76.15	75.50	33.01
108	93.05	93.50	37.62	83.88	83.25	36.30

5. CONCLUSIONS

Based on experimental studies and numerical analyses, the mechanical properties of 3D prints made of PA6-CF depend on material preparation conditions and loading direction. The experimentally obtained material parameters, in most cases, deviated from the manufacturer's catalog data, with strength values usually lower than declared. This means that designing structural elements solely on catalog data can lead to an overestimation of their load-bearing capacity and, consequently, to premature failure of the printed elements.

The orthotropic nature of PA6-CF material produced by the FFF/FDM method manifests itself in the highest strength in the X and Y directions, corresponding to the printing plane. Significantly lower strength values were observed in the Z direction, which is associated with adhesion between successive material layers. The Z direction was found to be the most critical with respect to the risk of structural damage.

When the system was loaded at the rated motor torque of 48 Nm, the tensile strength limits were not exceeded in any of the analyzed directions for both the annealed and unannealed materials. This indicates that the structure maintains load-bearing capacity under nominal static loading conditions. Maximum stress values occurred in the area of contact between the coupling sleeve and the crosspiece and in the outer sleeve in the Z-axis direction.

At a peak load of 120 Nm, there was a risk of damage to the printed components. For the unannealed material, the tensile strength limits were exceeded in the X and Y directions, while in both material variants, the Z direction exceeded the limit. This suggests that interlayer bonding may be a critical factor governing the potential failure of the analyzed components.

Design analysis conducted for torques ranging from 58 Nm to 108 Nm showed that, in the adopted numerical model, a torque of approximately 88 Nm did not cause the tensile strength limits to be exceeded. At this value, stresses in any of the analyzed directions do not exceed the allowable tensile strength. At higher loads, additional measures to enhance structural safety are necessary, such as annealing the printed components or limiting the motor's maximum torque in the control system.

The results also indicate that annealing the material improves strength in the X and Y directions but does not eliminate the low strength in the Z direction. Therefore, when designing elements printed with PA6-CF, special attention should be paid to print orientation and stress distribution relative to the direction of layer deposition. Further work should include tests on a larger number of specimens and experimental validation of the complete joint under operational loading conditions. The validation will involve comparing experimentally measured strains and critical failure locations with the numerical predictions obtained from the FEM model.

REFERENCES

1. Ficht G, Behnke S. Bipedal humanoid hardware design: a technology review. Current Robotics Reports. 2021;2:201–210. https://doi.org/10.1007/s43154-021-00050-9
2. Malvezzi M, Baldi TL, Villani A, Ciccarese F, Prattichizzo D. Design, development, and preliminary evaluation of a highly wearable exoskeleton. 2020 29th IEEE International Conference on Robot and Human Interactive Communication (RO-MAN). 2020;1055–1062. https://doi.org/10.1109/RO-MAN47096.2020.9223604
3. Hussain F, Goecke R, Mohammadian M. Exoskeleton robots for lower limb assistance: a review of materials, actuation, and manufacturing methods. Proceedings of the Institution of Mechanical Engineers, Part H: Journal of Engineering in Medicine. 2021;235(12):1375–1385. https://doi.org/10.1177/09544119211032010
4. Śpiewak S, Wojnicz W, Awrejcewicz J, Mazur M, Ludwicki M, Stańczyk B, Zagrodny B. Modeling and strength calculations of parts made using 3D printing technology and mounted in a custom-made lower limb exoskeleton. Materials. 2024;17(14):3406. https://doi.org/10.3390/ma17143406
5. Kussmaul R, Biedermann M, Pappas GA, Jónasson JG, Winiger P, Zogg M, Türk DA, Meboldt M, Ermanni P. Individualized lightweight structures for biomedical applications using additive manufacturing and carbon fiber patched composites. Design Science. 2019;5:e20. https://doi.org/10.1017/dsj.2019.19
6. Alqahtani MS, Al-Tamimi A, Almeida H, Cooper G, Bartolo P. A review of the use of additive manufacturing to produce lower-limb orthoses. Progress in Additive Manufacturing. 2020;5:85–94. https://doi.org/10.1007/s40964-019-00104-7
7. Prashar G, Vasudev H, Bhuddhi D. Additive manufacturing: expanding 3D printing horizon in Industry 4.0. International Journal on Interactive Design and Manufacturing. 2023;17:2221–2235. https://doi.org/10.1007/s12008-022-00956-4
8. Batkuldinova K, Abilgaziyev A, Shehab E, Ali MH. The recent development of 3D printing in developing lower-leg exoskeleton: a review. Materials Today: Proceedings. 2021;42:1822–1828. https://doi.org/10.1016/j.matpr.2020.12.191
9. Torrado AR, Shemelya CM, English JD, Lin Y, Wicker RB, Roberson DA. Characterizing the effect of additives to ABS on the mechanical property anisotropy of specimens fabricated by material extrusion 3D printing. Additive Manufacturing. 2015;6:16–29. https://doi.org/10.1016/j.addma.2015.02.001
10. Yasa E, Ersoy K. Dimensional accuracy and mechanical properties of chopped carbon reinforced polymers produced by material extrusion additive manufacturing. Materials. 2019;12(23):3885. https://doi.org/10.3390/ma12233885
11. Matsika Klossa C, Chatzidai N, Karalekas D. Tensile properties of 3D printed carbon fiber reinforced nylon specimens. Materials Today: Proceedings. 2023;93:571–574. https://doi.org/10.1016/j.matpr.2023.02.107
12. Kurkin E, Spirina M, Espinosa Barcenas O, Kurkina E. Calibration of the PA6 short-fiber reinforced material model for 10% to 30% carbon mass fraction mechanical characteristic prediction. Polymers (Basel). 2022;14(9):1781. https://doi.org/10.3390/polym14091781
13. Liao G, Li Z, Cheng Y, Xu D, Zhu D, Jiang S, Guo J, Chen X, Xu G, Zhu Y. Properties of oriented carbon fiber/polyamide 12 composite parts fabricated by fused deposition modeling. Materials&Design. 2018;139:283–292. https://doi.org/10.1016/j.matdes.2017.11.027
14. Polymaker. PolyMide PA6-CF technical data sheet [Internet]. [cited 2024 May 6]. Available from: https://polymaker.com/wp-content/uploads/lana-downloads/PolyMide_PA6_CF_TDS_V5.2.pdf

DOI: 10.65731/ama/2026-0075

Dawid Cekus: https://orcid.org/0000-0002-5551-1153

Tomasz Domański: https://orcid.org/0000-0002-5375-5402

Marcin Skotniczny: https://orcid.org/0000-0002-1514-7457

Paweł Kwiatoń: https://orcid.org/0000-0002-0067-0384

Jolanta Pozorska: https://orcid.org/0000-0001-6467-8142